arXiv:1612.00004v1 [cond-mat.supr-con] 30 Nov 2016

Kelvin-Helmholtz instability of AB interface in superfluid ^{3}He

V.B. Eltsov[1], A. Gordeev[1], M. Krusius[1]

[1] *Department of Applied Physics, Aalto University, P.O. Box 15100, FI-00076 AALTO, Finland*

(Dated: December 2, 2016)

The Kelvin-Helmholtz instability is well-known in classical hydrodynamics, where it explains the sudden emergence of interfacial surface waves as a function of the velocity of flow parallel to the interface. It can be carried over to the inviscid two-fluid dynamics of superfluids, to study different types of interfaces and phase boundaries in quantum fluids. We report measurements on the stability of the phase boundary separating the two bulk phases of superfluid ^{3}He in rotating flow, while the boundary is localized with the gradient of the magnetic field to a position perpendicular to the rotation axis. The results demonstrate that the classic stability condition, when modified for the superfluid environment, is obeyed down to $0.4\,T_c$, if a large fraction of the magnetic polarization of the B-phase is attributed to a parabolic reduction of the interfacial surface tension with increasing magnetic field.

Key words: superfluid ^{3}He, hydrodynamic instability, phase boundary, quantized vortex, vortex dynamics, interfacial surface tension

PACS numbers: 67.30hp, 47.20.Ft, 03.75.Kk, 97.60.Jd, 26.60-c

I. INTRODUCTION

The Kelvin-Helmholtz instability (KH) is one of the many celebrated instabilities of fluid flow [2], well-known in classical hydrodynamics since the 1860s [3, 4]. The traditional example is described by two horizontal fluid layers of different densities and different velocities parallel to their common interface. This state of relative laminar shear flow is stable at low velocities, *i.e.* the interface remains flat and smooth, but an instability develops when the difference in the velocities reaches a critical value. Originally the two flows were assumed inviscid, but ever since the incorporation of viscous effects has proven problematic. Thus the connection remains complicated between the inviscid model and the countless manifestations of the KH instability of different systems observed in nature.

The instability of the interface separating the two bulk-liquid phases of superfluid ^{3}He, the A and B phases, is one of the most extraordinary superfluid examples [5] and now a prime laboratory show case of the KH theory [6]. The AB interface is a sharp boundary in the distribution of the order parameter of the superfluid state, with a width on the order of the superfluid coherence length. The flow of the superfluid components of the A and B superfluids can be truly inviscid, but to account for the coupling with the normal component, which provides the connection to a fixed reference frame, the instability condition has to be reformulated. In ^{3}He studies the instability has found many useful applications, foremost in measurements of quantized vortex dynamics. The goal of this report is to review the agreement between the instability condition and the superfluid measurements.

II. KH INSTABILITY IN SUPERFLUID ^{3}HE

The KH measuring arrangement is illustrated in Fig. 1. The two-phase configuration with a stable AB interface can be set up in a long cylinder in an inhomogeneous magnetic field which exceeds the critical field $H_{\rm AB}(T,P)$ where ^{3}He-A becomes energetically preferable to ^{3}He-B. The initial state in rotation is engineered to have the equilibrium number of quantized vortices in the A phase, providing its solid-body-like rotation, while the superfluid component in the B phase is vortex free and thus non-rotating (stationary in the laboratory frame). This meta-stable non-dissipative state persists to relatively high rotation, until at a critical velocity of the relative tangential flow velocities an interfacial mode is excited and a number of vortices from the A phase manage to cross into the B phase. The sudden appearance of B-phase vortices is the experimental signal for the instability. Its dependence on rotation, temperature, and pressure is measured in these experiments.

The meta-stable starting situation requires special preparation. Initially at rest at constant temperature, the cylinder is slowly accelerated to rotation until some constant angular velocity Ω which is below the critical velocity Ω_c of the KH instability. The A-phase section has by then become filled with rectilinear doubly-quantized vortices [7]. These have an extended core with a continuous order parameter distribution and thus a very low critical rotation velocity. At the AB interface the double-quantum cores dissociate, bend parallel to the interface, and extend radially out to the cylinder wall, forming a vortex sheet on the interface [8]. In contrast, the B phase section remains vortex free. This configuration remains meta-stable largely because energetically a sizeable local concentration of kinetic energy is required to convert the two orders of magnitude fatter core of the A-phase double-quantum vortex to a lean

single-quantum B-phase core with singular structure and a radius comparable to the superfluid coherence length $\xi_0 \propto \hbar v_F/(k_B T_c) \gtrsim 10\,\mathrm{nm}$ (where v_F is the Fermi velocity and T_c the superfluid transition temperature).

Next the rotation drive Ω is increased by a small increment $\Delta\Omega \ll \Omega$ to Ω_c or slightly above. Here the phase boundary cannot support any more the discontinuity in the tangential flow velocities across the interface and a damped surface wave is triggered. It unleashes the escape of a variable number of vortex quanta $\kappa = h/(2m_3)$ through the AB interface in the form of a small bundle of closely packed vortex loops, which all are embedded within one surface depression of the interfacial wave. At high temperatures $T > 0.6\,T_c$ the large friction in vortex motion limits interactions among the loops, the number of individual vortices in the bundle remains constant, and they ultimately grow to rectilinear vortex lines. In the final state these are arranged as a central cluster of rectilinear singly-quantized B-phase vortices with a singular topological "boojum" point defect at the AB interface where they connect to dissociated halves of the A-phase double-quantum vortex [9].

Towards lower temperatures the damping of vortex motions, the "mutual friction" $\alpha(T,P)$, radically decreases. Below $0.6\,T_c$, $\alpha \lesssim 1$ and the B phase enters the turbulent regime. Here the number of vortex quanta in the escaping bundle is not conserved while the small loops evolve to rectilinear B-phase vortex lines. Instead the loops interact and proliferate via reconnections to a turbulent burst [10]. In the rotating counterflow the turbulent burst is rapidly turned [11] into a rotating state with rectilinear vortices close to the equilibrium number of lines $N_{eq} = \pi R^2 n_v$ (here R is the radius of the cylinder and $n_v = 2\Omega/\kappa$ the areal density of rectilinear lines in the B-phase vortex array in solid-body rotation).

The experimental signal of the instability is the change in the B-phase vorticity, which is monitored non-invasively with continuous-wave NMR spectrometers. Their detector coils are located outside the rotating cylinder above and below the interface, in A and B-phase sections residing in homogeneous axially oriented polarizing magnetic fields.

The instability at Ω_c proves to be reproducible and to depend on temperature T, on the externally applied pressure P to which the ^{3}He sample has been pressurized, and on the current I_b in the solenoid magnet which creates the inhomogeneous magnetic field for localizing the AB phase boundary. Owing to its well-behaved critical properties, the superfluid KH instability has frequently been made use of as a tool to investigate superfluid dynamics. For instance, it can be used as an injection method by which a small bundle of vortex seed loops is ejected in applied counterflow to study the evolution of the seeds [12].

The superfluid KH instability was perhaps first invoked as an explanation for the threshold to capillary wave formation on the free surface of a bath of superfluid ^{4}He [13]. It has also been proposed as a tool to explore the interface of the superfluid dilute ^{3}He-^{4}He liquid mixture with its normal concentrated phase [14]. More recently a flurry of theoretical investigations has appeared which recommend the KH instability as a means to study mixtures of different cold-atom Bose-Einstein condensates (see eg. [15–18]). Another intriguing suggestion is to use the KH instability for modelling a hydrodynamic analogue of the event horizon of a gravitational black-hole singularity, since the instability involves flows at different velocities: the velocities of the mass shear flows along the interface and the velocity of the surface wave excited on the interface [19, 20].

The superfluid KH instability has also emerged as one of the possible mechanisms by which a sudden equilibrium could be reached in one "glitch" between the angular momentum reservoirs of the superfluid and normal fractions of a spinning neutron star [21]. The sudden discontinuous glitch-like "spin-up event" in the neutron star's rotation velocity was found to match in magnitude the angular velocity jump which one might expect in a typical KH instability event when the outward directed motion of quantized vortices across an interface between two different neutron condensates is calculated. New estimates of the superfluid fraction and its degen-

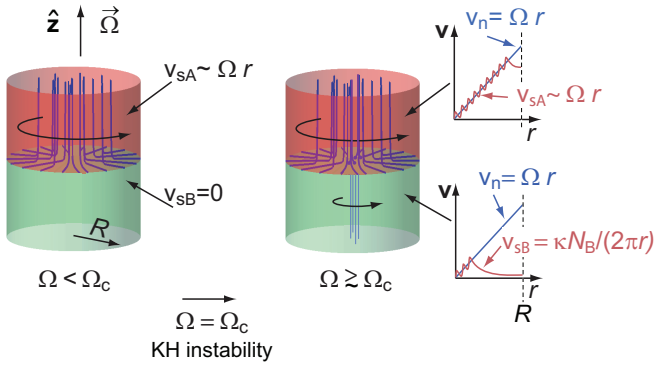

FIG. 1: KH instability in superfluid ^{3}He. The two bulk phases of superfluid ^{3}He can coexist in a cylinder rotating at constant angular velocity Ω in an inhomogeneous axially oriented "barrier" magnetic field $H_b(z)\hat{z}$. The interface is at the location z_0, where $H_b(z_0) = H_{AB}(T,P)$: in the high-field region $H_b \geq H_{AB}$ A phase is stable while at lower fields $H_b \leq H_{AB}$ B phase is stable. ***(Left)*** When Ω is increased at constant temperature from zero to some value less than $\Omega_c(T,P,I_b)$, the A-phase section is filled with rectilinear double-quantum vortices at the equilibrium density Ω/κ. At the AB interface these curve to form a vortex sheet covering the interface, leaving the B-phase section vortex free. ***(Right)*** When Ω is increased past Ω_c, the KH instability mediates the transfer of a bundle of small vortex loops through the AB interface into the B-phase. In the temperature regime of laminar flow above $0.6\,T_c$ these grow to rectilinear single-quantum vortices which extend across the AB interface and form a cluster at the equilibrium density $2\Omega/\kappa$ in the centre of the cylinder (as shown here). In the turbulent regime below $0.6\,T_c$ the loops interact in a turbulent burst, filling the B-phase section ultimately with the equilibrium number of rectilinear vortices.

eracy temperature in the interior of a spinning neutron star indicate that superfluidity extends across the boundary of the inner crust and the central core [22]. Unfortunately, the phase diagram of neutron superfluids in a strong density gradient much above nuclear densities is largely unknown. Moreover, the spherical geometry of the neutron star's interior complicates the KH response from that of the simple example in Fig. 1. This is illustrated by superfluid ^{3}He measurements where the AB interface is a near concentric cylindrical surface within the rotating cylinder [23]. Nevertheless, the KH instability remains a plausible option in the neutron-star glitch problem.

This report recapitulates an overview of the superfluid Kelvin-Helmholtz instability at the AB phase boundary, starting with a reminder about its analytical definition in Sec. III and about experimental aspects in Sec. IV. For further details about these matters we refer to Ref. [24]. The results from so far unpublished measurements on the critical rotation velocity Ω_c as a function of the three variables T, P and I_b are summarized in Sec. V. In Sec. VI the more general implications from the analysis are discussed. The results display good agreement between experiment and theory – at higher temperatures without fitting parameters – for a phenomenon which is not trivial either experimentally or theoretically. This harmony illustrates the power of the ^{3}He superfluids as quantum model systems.

III. KH THEORY

The classic example of the KH-instability is at the horizontal interface of two inmiscible and inviscid fluid layers with densities ρ_1 and ρ_2. Assigning v_1 and v_2 as the corresponding flow velocities parallel to the interface, the instability develops when the relative velocity $\mid v_1 - v_2 \mid$ satisfies Lord Kelvin's condition [3]

$$\frac{\rho_1\rho_2}{\rho_1+\rho_2}(v_1-v_2)^2 = 2\sqrt{\sigma F}, \qquad (1)$$

where the interface is characterized by its surface tension σ and its restoring force F which often is the gravitational force $F = g \mid \rho_2 - \rho_1 \mid$. The interface becomes unstable when the free energy of the perturbed interface drops below that of the flat surface and an interfacial capillary wave is formed with the wave vector

$$k_0 = \sqrt{F/\sigma}\ . \qquad (2)$$

A. Instability at low magnetic field

In transferring the classical result to an interface separating two superfluids, the dissipative motion of the AB interface needs to be taken into consideration: Andreev scattering of quasiparticles from the interface leads to heavily damped interface motion [25, 26]. This constraint introduces a third velocity in the instability condition, namely the velocity of the viscous normal components. These couple the superfluid fractions to the reference frame of the cylinder rotating at constant angular velocity Ω, where solid-body corotation with the container walls is preferred. Thus the instability condition has to be recast in the Galilean invariant form [6]

$$\frac{1}{2}\rho_{s1}\ (v_{s1}-v_n)^2 + \frac{1}{2}\rho_{s2}\ (v_{s2}-v_n)^2 = \sqrt{\sigma F}\ . \qquad (3)$$

We see here that the superfluid instability becomes possible also when the relative superfluid velocity vanishes, when $v_{s1} = v_{s2}$ and the two streams parallel to the interface flow at the same velocity. The rigidity of the AB interface is maintained by the inter-phasial surface tension σ and the restoring force F arising from the inhomogeneous magnetic stabilizing field: $F = \frac{1}{2}\,(\chi_A - \chi_B)\,\nabla H^2 \approx (\chi_n - \chi_B)\,H_z\,(dH_z/dz)$. The deformation of the interface starts with the wave vector k_0 given by Eq. (2).

A simplification can be introduced in Eq. (3) since the critical velocity of spontaneous vortex formation in the A phase is low, of order 0.1 rad/s [27], while in the B phase it is higher at $\gtrsim 2$ rad/s, depending on the smoothness of the quartz cylinder wall [28]. We approximate the A phase as being in the equilibrium rotating state, $\mathbf{v}_{sA} \approx \mathbf{\Omega}\times\mathbf{r} = \mathbf{v}_n$ (in the laboratory coordinate system), so that only the flow velocity in the vortex-free B phase counts: $\mathbf{v}_{sB} = -\mathbf{\Omega}\times\mathbf{r}$ (in the rotating coordinate system). Eq. (3) is thereby reduced to

$$\Omega_c^2 = 2\frac{\sqrt{\sigma F}}{\rho_{sB}\ R^2}\,. \qquad (4)$$

Here ρ_{sB} is the density of the superfluid component in the B phase at the interface. Note that compared to the corresponding value from Eq. (1) for the ideal inviscid fluid, Ω_c^2 in Eq. (4) is smaller by a factor of 2. For analysing measurements, the instability criterion can be divided in predominantly experimental or theoretical parts, w_{exp} and w_{theo},

$$w_{exp} = \frac{(\Omega_c\,R_{eff})^4}{2\,[\nabla H^2]_{H=H_{AB}}} = \frac{\sigma\ \Delta\chi}{\rho_{sB}^2} = w_{theo}\,. \qquad (5)$$

Here $R_{eff} = v_{sB}^c/\Omega_c$ is used for the radial location of the instability site at the interface. In Ref. [8] it was experimentally determined to be situated somewhat displaced from the cylinder wall, effectively at $R_{eff} \approx 0.87\,R$. The left side of Eq. (5) contains the quantities which are here experimentally determined, while on the right the three quantities σ, $\Delta\chi = \chi_A - \chi_B$, and ρ_{sB} have to be obtained from the literature or from calculations.

From Eqs. (2) and (4) the wave length λ of the overdamped interfacial excitation mode created at the instability is seen to be

$$\lambda = 4\pi\ \frac{\sigma}{\rho_{sB}}\ (\Omega_c\,R_{eff})^{-2}\,. \qquad (6)$$

A second estimate describes this quantity from another point of view. The instability is signaled by the transfer

of vortices across the interface, when vortex loops escape from an interfacial surface wave depression which protrudes in the B-phase. Initially the escaping vortices are part of the interfacial vortex sheet and coat the surface wave depression, *i.e.* the number ΔN of these vortex loops is that which fits in one half of the wave length λ of the surface excitation mode. The instability is a complex non-equilibrium event, but the escaping circulation ΔN is well-defined with a measurable statistical distribution function [12].

This can be confirmed at temperatures above the transition to turbulence, $T > 0.6\,T_c$, where the number of loops expanding in the B-phase section to rectilinear vortex lines is conserved and thus can be counted in the final state after the instability. The number of circulation quanta, which in the interfacial vortex sheet flare out to the cylinder wall, is $N_{eq} \approx \pi R^2(2\Omega_c/\kappa)$. Per unit length measured along the perimeter one then has $\sim R\,\Omega_c/\kappa$ quanta flaring radially outward so that one half of the wave length of the surface wave fits $\Delta N \approx \frac{1}{2}\lambda\, R_{\rm eff}\,\Omega_c/\kappa$ quanta. Taking numbers pertinent for Fig. 4, we arrive at an estimate $\lambda \sim 0.4\,$mm.

Measurements on the instability in Eq. (4) are locked to the AB interface at the critical field $H_{\rm AB}(T,P)$. They are conducted at constant pressure, by either scanning temperature or the magnetic field gradient at constant temperature (*i.e.* by changing I_b). At constant pressure P, $H_{\rm AB}$ traces a near parabolic curve in the $H-T$ plane in the present experimental range, approaching values as large as $\lesssim 0.6\,$Tesla at the lowest temperatures. Using currently accepted values for the superfluid ^{3}He properties at low fields, good agreement is found with Eq. (4) at high temperatures above about $T/T_c > 0.7...0.8$, corresponding to $H_{\rm AB} \lesssim 0.1\,$Tesla [5]. At lower temperatures the magnetic polarizability of the B phase reduces the stability of the AB interface and the measured Ω_c falls increasingly below that calculated with low-field values (see illustration *eg.* in Fig. 14 of Ref. [24]). At $\sim 0.4\,T_c$ the difference is of order $\sim 0.1\,\Omega_c$.

B. Magnetic field dependence

The magnetic field $H_{\rm AB}(T,P)$ increases monotonicly towards low temperatures and introduces changes in the B-phase properties which reduce the interface stability. The Ginzburg-Landau (GL)expansion of the magnetic-field-induced gap deformation is in first order parabolic $(\Delta_\parallel/\Delta_{B0})^2 \approx 1 - 2\,a_1H^2\,(1-T/T_c)$ and $(\Delta_\perp/\Delta_{B0})^2 \approx 1 + \frac{1}{4}a_1H^2\,(1-T/T_c)$ which scales with pressure as $a_1 \propto T_c^2$ [29]. The corresponding suppression of the axial component of *eg.* the superfluid density is $\rho_{s\parallel}/\rho_{B0} = 1 - a_2H^2/(1-T/T_c) + ...$, where $a_2 \propto a_1$. Little quantitative information exists on the field dependences of the relevant B-phase properties at temperatures below the GL regime, but the changes can be estimated with numerical weak coupling calculations [30, 31]. At zero pressure in the zero-temperature limit such calculations give a gap distortion [31] which agrees well with vibrating wire measurements on the onset of pair-breaking as a function of the applied magnetic field, as reported by Shaun Fisher *et al.* [32]. In comparison the depairing and gap suppression expected from superfluid flow is small in the range of the present KH measurements.

In addition, magnetic fields affect B-phase textural orientations and require a reconsideration of the boundary conditions at the AB interface. Generally in B-phase the order parameter texture has less of an influence on the hydrodynamic stability than in the A phase, where the texture at the wall of the rotating cylinder determines *eg.* the critical flow velocity of vortex formation [27]. Nevertheless, orientational considerations lead to corrections which can be built into Eq. (4) in terms of a renormalized superfluid density $\rho_{s,\rm eff}$ [33].

At the interface one requires 1) continuity of mass flow $\boldsymbol{\nabla}\cdot(\overleftrightarrow{\rho}_{sB}\cdot\mathbf{v}_{sB}) = 0$ and 2) stability of the phase boundary such that no mass flow takes place through the interface in the direction of its unit normal $\hat{\mathbf{s}}$, *i.e.* $\hat{\mathbf{s}}\cdot(\overleftrightarrow{\rho}_{sB}\cdot\mathbf{v}_{sB}) = 0$. Writing the B phase mass density tensor in the form $\overleftrightarrow{\rho}_{sB} = \overleftrightarrow{\rho}_s = \rho_x\ \hat{\mathbf{x}}\hat{\mathbf{x}} + \rho_y\ \hat{\mathbf{y}}\hat{\mathbf{y}} + \rho_z\ \hat{\mathbf{z}}\hat{\mathbf{z}}$ and choosing the cartesian coordinate $\hat{\mathbf{x}}$ to lie along the flow and along the interface while $\hat{\mathbf{z}}$ is the direction perpendicular to the interface, then Eq. (4) can be amended in the form

$$\Omega_c^2 = 2\frac{\sqrt{\sigma F}}{\rho_{s,\rm eff}\ R^2}\,, \tag{7}$$

where the superfluid density ρ_{sB} has been replaced by an effective quantity,

$$\rho_{s,\rm eff} = \rho_x\sqrt{\rho_x/\rho_z}\,. \tag{8}$$

The magnetic-field-distorted B-phase superfluid density is of the symmetric uniaxial form

$$\rho_{ij} = \rho_\parallel\ \hat{\ell}_i\,\hat{\ell}_j + \rho_\perp\ (\delta_{ij} - \hat{\ell}_i\,\hat{\ell}_j), \tag{9}$$

where the anisotropy axis (the gap axis) lies along the unit vector $\hat{\boldsymbol{\ell}} = \hat{\mathbf{H}}\cdot\bar{\mathbf{R}}$, the unit vector $\hat{\mathbf{H}} = \mathbf{H}/H$ points in the direction of the applied field $\mathbf{H}$, and $\bar{\mathbf{R}}(\hat{\mathbf{n}},\theta)$ is a rotation matrix which rotates around the axis $\hat{\mathbf{n}}$ by the angle $\theta = \arccos(-\frac{1}{4}\Delta_\parallel/\Delta_\perp)$.

A number of interactions act to orient the anisotropy axis $\hat{\boldsymbol{\ell}}$, giving rise to an order parameter texture $\hat{\boldsymbol{\ell}}(\boldsymbol{r})$, which is of the axially symmetric 'flare-out' configuration in a long cylinder with bulk B phase. At moderate magnetic fields in the regime of typical NMR measurements [34], the 'flare-out' textures have been examined in numerous studies and the magnitude of the various textural interactions is well documented [35]. This applies to the B-phase textures within the two NMR detector coils in Fig. 2, where the field is of order $H \sim 30\,$mT, *i.e.* well above the field $H_D \gtrsim 1\,$mT corresponding to the dipolar spin-orbit interaction, but well below the critical field $H_{\rm AB}$ needed for stabilizing the AB interface. The flare-out texture is formed by the coupling to the

magnetic field, to rotation, and by the boundary condition at the cylinder wall. Owing to the presence of a gradient energy, in spatially inhomogeneous conditions these interactions have a characteristic range or 'healing length'. These lengths have been measured in low-field NMR conditions, but at high fields of order of H_{AB}, texture studies require high field homogeneity and become experimentally demanding. It is not accurately known what is the relative range of the interactions determining the configuration of $\hat{\boldsymbol{\ell}}(\boldsymbol{r})$ in the vicinity of the AB interface and what alignment therefore should be assigned to $\rho_{\rm s,eff}$ in Eq. (8).

Close to the interface one finds regions in the B-phase texture where the orientation can be along any of the cartesian axes x, y, and z. As the dominant orienting interaction is the magnetic field, the gap axis is predominantly aligned parallel to the field, $\hat{\boldsymbol{\ell}} = \hat{\mathbf{H}} = \hat{\mathbf{z}}$, and the effective B-phase superfluid density in Eq. (8) becomes

$$\rho_{\hat{\boldsymbol{\ell}}\|\hat{\mathbf{z}}} = \rho_\perp \sqrt{\rho_\perp/\rho_\parallel}\,. \tag{10}$$

Since the isotropic zero magnetic field superfluid density $\rho_{\rm s0} \approx \rho_\perp > \rho_\parallel$, the effective superfluid density in Eq. (7) is magnified: $\rho_{\hat{\boldsymbol{\ell}}\|\hat{\mathbf{z}}} > \rho_{\rm s0}$. In the high-fields close to the interface the alignment $\hat{\boldsymbol{\ell}} \parallel \hat{\mathbf{z}}$ is expected to prevail and to occupy most of the flare-out texture. Right at the interface on the other hand, the boundary condition on $\hat{\boldsymbol{\ell}}$ requires parallel alignment to the AB interface [8]. To minimize the flow energy, $\hat{\boldsymbol{\ell}}$ will then also align itself along the flow, $\hat{\boldsymbol{\ell}} = \hat{\mathbf{x}}$, and

$$\rho_{\hat{\boldsymbol{\ell}}\|\hat{\mathbf{x}}} = \rho_\parallel \sqrt{\rho_\parallel/\rho_\perp}\,. \tag{11}$$

In this part of the texture, the effective superfluid density is reduced: $\rho_{\hat{\boldsymbol{\ell}}\|\hat{\mathbf{x}}} < \rho_{\rm s0}$. Alignment along the third cartesian axis, $\hat{\boldsymbol{\ell}} = \hat{\mathbf{y}} = \hat{\mathbf{r}}$, is realized in a boundary layer at the cylinder wall, enforced by a boundary condition which orients $\hat{\boldsymbol{\ell}}$ perpendicular to the wall, so that

$$\rho_{\hat{\boldsymbol{\ell}}\|\hat{\mathbf{r}}} = \rho_\perp\,. \tag{12}$$

In this case the effective superfluid density remains practically unchanged from its low-field value since $\rho_\perp \gtrsim \rho_{\rm s0}$.

Hence the B-phase order parameter texture may influence the hydrodynamic stability of the AB interface. The magnetic healing length $\xi_H(T,H)$, the length scale on which $\hat{\boldsymbol{\ell}}$ bends from $\hat{\boldsymbol{\ell}} = \hat{\mathbf{H}} = \hat{\mathbf{z}}$ in the bulk to $\hat{\boldsymbol{\ell}} = \hat{\mathbf{x}}$ at the interface, is obtained by comparing the magnetic orientation energy density of order $[(\Delta_\parallel - \Delta_\perp)\Delta_\perp/H^2]\,(\hat{\boldsymbol{n}}\cdot\boldsymbol{H})^2$ to the gradient energy density, which resists distortions from uniform $\hat{\boldsymbol{\ell}}$ orientation.

At the low fields of conventional NMR measurements ξ_H is found to be $\propto 1/H$ and in magnitude a sizeable fraction of the sample cylinder radius R [36]. At higher fields accurate information on ξ_H is lacking. Recent measurements on the dissipation recorded while the AB interface is oscillated with an ac magnetic field were explained assuming the heating to arise from orbital viscosity of the oscillating $\hat{\boldsymbol{\ell}}$ orientation [37]. Good agreement with measured heating levels at different frequencies was obtained assuming a short healing length $\xi_H \sim 0.1\,$mm and a uniform bulk texture with $\hat{\boldsymbol{\ell}} = \hat{\mathbf{H}} = \hat{\mathbf{z}}$ in $H_{\rm AB} = 0.34\,$T magnetic field at zero pressure and $0.16\,T_{\rm c}$. This suggests that on moving away from the AB interface into bulk B phase the $\hat{\boldsymbol{\ell}}$ orientation recovers rapidly within a short distance $\ll R$ from being parallel to the interface to being oriented along the field.

The stability criterion Eq. (7) is thus expected to involve the length scales $R \gg R - R_{\rm eff} \sim \lambda > \xi_H$. This means that when the amplitude of the perturbations sampling the interface stability become comparable to λ, they have already exceeded ξ_H and the effective density increases to that in Eq. (10). This reduces the critical velocity $\Omega_{\rm c}$. The site of the instability becomes the spot in the texture where the required rotation velocity is the lowest. At intermediate temperatures the enhancement $\rho_{\rm s,eff}/\rho_{\rm s0}$ may be several percent and larger at low pressures, but at the lowest temperatures $\lesssim 0.2\,T_{\rm c}$ it vanishes exponentially. In contrast, owing to the parallel alignment $\hat{\boldsymbol{\ell}} = \hat{\mathbf{x}}$ at the interface, it is $\chi_\perp \approx \chi_{\rm B0}$ which enters in the magnetic restoring force F.

However, to explain the main contribution to the reduced interface stability at large fields, the changes in $\rho_{\rm sB}$ and $\chi_{\rm B}$ prove to be small compared to the reduction in the surface tension $\sigma(T,H,P)$. The interface tension is experimentally accessible only at the critical field $H_{\rm AB}(T,P)$. Being a sharp interface in the order parameter distribution with a width on the order of the superfluid coherence length $\xi(T,P) = \xi_0/\sqrt{(1-T/T_{\rm c})}$, the surface tension is of order $\sim \xi f_{\rm cB}$, where $f_{\rm cB}$ is the B-phase condensation energy. Its G-L expansion is of the form $\propto (1-T/T_{\rm c})^2[1 - a_3H^2/(1-T/T_{\rm c})]$ [38], so that the low-field surface tension is expressed as $\sigma(T,P) \approx \sigma_{\rm AB}(0,P)\,(1-T/T_{\rm c})^{3/2}$. Its calculation at low temperatures and high fields is a complex task, since one has to find the minimum-energy order parameter trajectory from A phase to the field-distorted B-phase energy minimum [39]. With increasing $H_{\rm AB}(T,P)$, the energy barrier is reduced and the surface tension decreases.

IV. EXPERIMENTAL METHOD

A. Measuring setup

Our KH measurements have been performed in the experimental setup of Fig. 2, a versatile platform for many different types of studies after the placement of apertures and sensors is varied. The heart of this setup is a fuzed quartz glass cylinder of 11 cm length and 0.6 cm inner diameter, which is used as sample container. A small superconducting solenoid around the middle section of

the long tube generates the magnetic field for stabilizing a layer of A phase which acts as a barrier between B-phase sections at each end of the tube. We call this the BAB stacking configuration of phases, in contrast to the metastable AB configuration where the entire top section above the lower AB interface is filled with A phase. Thus depending on magnetic field, temperature, pressure, and prehistory different configurations of A and B phases can be trapped in the cylinder.

Fig. 3 shows the highly peaked axial distribution of the barrier field. Here the magnetic field is rapidly changing both within and outside the A-phase barrier layer. In contrast, further away at both ends of the sample tube end-compensated solenoids create homogeneous polarizing fields for monitoring the superfluid order parameter field with low-field NMR spectrometers. This is the regime where experiment and theory of order parameter textures is well established [34]. In the resulting continuous-wave NMR signal, the amplitudes provide information about the number of vortices, while the frequency shifts of satellite peaks have been calibrated to provide the temperature scale for the measurements.

In rotation the section with A phase supports roughly the equilibrium number of vortices in the form of lines or sheets with continuous order parameter distributions (*i.e.* no singular vortex cores) and low critical rotation velocity ($\Omega_{\rm cA} \approx 0.1\,{\rm rad/s}$) for the formation of vorticity. Here it is the order parameter texture which controls the critical velocity and the type of vorticity to be formed [40].

In contrast, in the B-phase sections an important aspect is the surface quality of the inner cylinder wall, *i.e.* the critical velocity for the formation of singular-core vortices depends crucially on the smoothness of the wall. With careful cleaning and etching, combined with visual screening in a microscope, isolated surface defects can be eliminated which makes critical velocities $\Omega_{\rm cB} \gtrsim 2\,{\rm rad/s}$ possible. In addition careful cool-down procedures are required, to avoid frozen water or gas accumulations on the walls. Moreover, to isolate from contact with the rough sintered heat exchanger surface below the sample tube, the cylinder needs to be terminated with an orifice on the cylinder axis, which here has a diameter of 0.75 mm. The upper limit of vortex-free rotation, which corresponds to an apparent effective velocity of vortex formation, was measured at 33.7 bar pressure in the absence of the A-phase barrier layer (*i.e.* when $I_{\rm b} = 0$). It proved to have a temperature independent value of $(2.2 \pm 0.25)\,{\rm rad/s}$ in the range 0.55 — $0.75\,T_{\rm c}$. Thus KH instabilities, where the first event occurs above this value, would not be accessible with this sample cylinder.

The obvious drawback from the orifice is the large thermal resistance which it presents for axial heat flow. Heat leaks of order $\sim 100\,{\rm pW}$ flowing from the sample cylinder through the orifice to the much colder heat exchanger volume (maintained at roughly $0.14\,T_{\rm c}$) limit the lowest achievable temperature to $\sim 0.20\,T_{\rm c}$ in the experimental volume above the orifice.

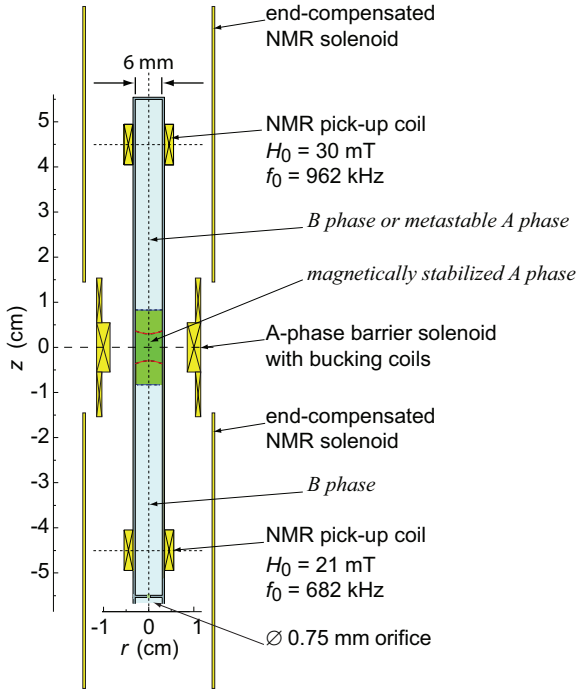

FIG. 2: Measurement of KH instability. The liquid ^{3}He sample is contained in a long quartz glass cylinder with smooth walls. The section in the middle is magnetically maintained in the A phase, while NMR detectors with single-vortex measuring resolution are located at both ends of the cylinder. The axially oriented magnetic fields are generated with superconducting solenoids [41] which are thermally connected to the mixing chamber of the dilution refrigerator, used for precooling the copper nuclear cooling stage. A division plate with a small aperture separates the experimental volume from the thermal connection to the nuclear cooling stage, a sintered heat exchanger with rough surfaces. Two examples of AB interfaces are shown at 29 bar pressure and $0.55\,T_{\rm c}$: the inner concave phase boundaries are stabilized with a current $I_{\rm b} = 4\,{\rm A}$ in the barrier solenoid and the outer flatter boundaries with $I_{\rm b} = 8\,{\rm A}$.

B. Measuring procedures

With continuous wave excitation the entire NMR line can be displayed by sweeping the polarization field. In a KH instability event the line shape changes discontinuously, as some NMR absorption is shifted from the high-field edge of the signal to the Larmor edge at low-field, while the total integrated NMR absorption remains constant. As shown in Fig. 4, a prominent NMR signal can be retrieved from a single instability event. In this figure the NMR absorption is recorded continuously close to the Larmor edge, where the absorption increases discontinuously when the rotation velocity is increased at a slow rate past the consecutive KH instabilities. The first signal discontinuity defines the KH critical rotation velocity $\Omega_{\rm c}$, while the succession of the following new instability

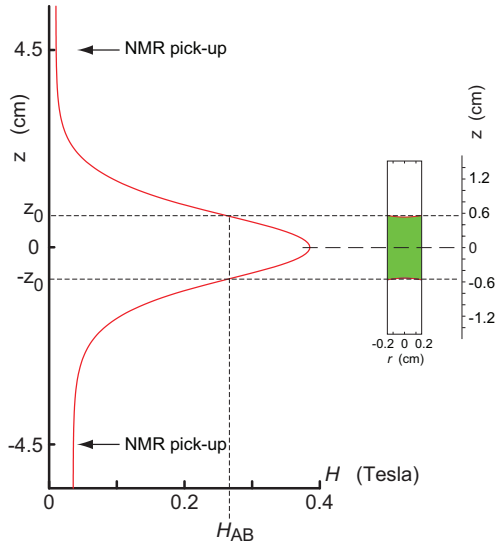

FIG. 3: Axial distribution of the barrier magnetic field at $I_b = 4\,\mathrm{A}$ **(on the left)**. **On the right** the A-phase layer in the BAB configuration is shown at 29 bar pressure, 1.62 mK $= 0.67\,T_c$, and $H_{AB} = 0.276\,\mathrm{mT}$. The calculated shape of the concave AB interface meniscus [42] is mainly determined by the magnetic energy (owing to $\Delta\chi = 5.25 * 10^{-8}$ cgs) in the solenoidal field which increases radially, but also to a smaller extent by the surface tension $\sigma_{AB} = 9.3\,\mu\mathrm{erg/cm^2}$, by vortex-free rotation at 1 rad/s in the B-phase sections and an equilibrium vortex state in the A layer (with vortex formation starting at $\Omega_{cA} = 0.15\,\mathrm{rad/s}$). The contact angle at the cylinder wall is fixed to $\theta_{AB} = 68^\circ$.

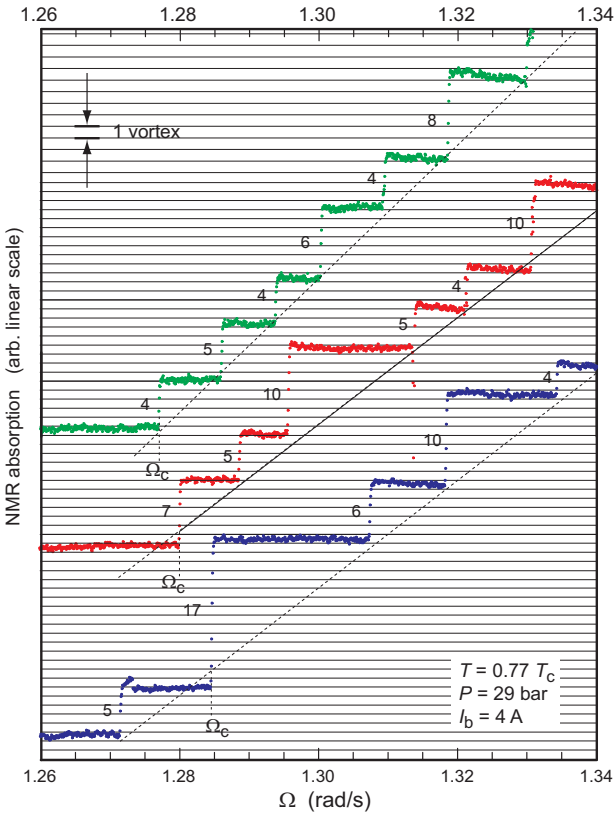

FIG. 4: NMR signal from KH measurements. Three series of measurements are shown as a response to a slow increase of rotation at a rate of $2 * 10^{-4}\,\mathrm{rad/s^2}$. This is slow enough to maintain near equilibrium conditions. The NMR output plotted on the vertical axis monitors the absorption level at the Larmor edge of the NMR spectrum. This is the location from where the absorption starts during an upward sweep of the NMR polarizing field and where the absorption is concentrated in the equilibrium vortex state. In vortex-free rotation at $\Omega < \Omega_c$ the NMR absorption is shifted almost entirely in a counterflow peak at higher NMR field. The vortices ΔN created in a KH event shift part of the absorption back to the Larmor edge. At small vortex numbers $N \ll N_{eq}$ the changes in absorption from the counterflow peak to the Larmor edge are approximately $\propto \Delta N$, as illustrated by the grid where the spacing corresponds to one vortex. The numbers next to each KH discontinuity give ΔN. The scatter in the critical points illustrates the stability of the measurement and not fluctuations in the KH instability.

events defines the critical line

$$v_c = \Omega_c\, R_{\mathrm{eff}} = \left(\Omega - \frac{\kappa\, N(\Omega)}{2\pi R_{\mathrm{eff}}^2}\right) R_{\mathrm{eff}}\,, \qquad (13)$$

where the KH critical flow velocity v_c is a constant and $N(\Omega)$ is the number of vortices which have broken through the AB interface by the time rotation has been increased to the value $\Omega \geq \Omega_c$. The dashed line has been fitted to the critical end points of the staircase pattern and provides the slope $\Delta N/\Delta\Omega = 2\pi R_{\mathrm{eff}}^2/\kappa$ which yields $R_{\mathrm{eff}} = \sqrt{\frac{\kappa}{2\pi}\frac{\Delta N}{\Delta\Omega}} \approx 2.5\,\mathrm{mm}$. It should be compared to the cylinder radius $R = 3\,\mathrm{mm}$.

As seen in Fig. 4, the number of circulation quanta ΔN can be even or odd. Thus, despite the fact that the A phase is arranged to be filled with doubly-quantized vortex lines, the circulation covers the AB interface on the A-phase side as a vortex sheet which is made up of vorticity in dissociated form. On an average one finds that $\Delta N \approx 8$ [8]. In the BAB stacking configuration, the instabilities of the two AB interfaces occur independently and randomly, but follow the same critical line. The scatter of the critical points in Fig. 4 is related to the stability of the measuring conditions, *i.e.* better controlled measurement procedures lead to more precise results. Hence the instability appears to be highly predictable, inherent fluctuations are not measured with current means, and the limitations on the measurements in Fig. 4 seem to be caused by long-term drifts. These are minimized by adjusting continuously for changes in temperature and pressure. Moreover, instead of monitoring continuously the NMR amplitude at fixed frequency shift (as in Fig. 4), the precision in determining ΔN can be improved by recording the entire NMR line shape at constant rotation just before and after triggering an instability event with an incremental rotation increase by $\Delta\Omega$.

The response time of the measurement is limited by

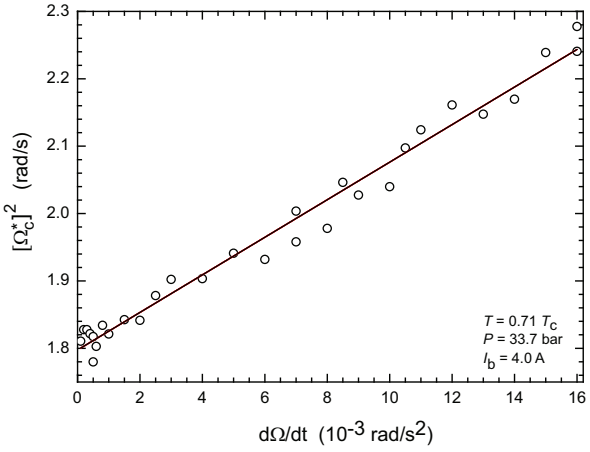

FIG. 5: Response time of KH measurement. For each data point rotation is increased from zero at constant rate $\dot\Omega$, plotting the square of the apparent KH critical velocity Ω_c^* as a function of the rate $\dot\Omega$, while $T = 0.71\,T_c$, $P = 33.7\,\mathrm{bar}$, and $I_b = 4\,\mathrm{A}$ are maintained constant. The vertical intercept gives the true critical velocity Ω_c and the slope the dissipative vortex mutual friction coefficient α. The lowest data point $[0.5\times10^{-3}, 1.33\,\mathrm{rad/s}]$ was recorded while the A-phase vortex structure was the vortex sheet. Within the scatter, it agrees with the results from all other measurements where the A-phase section was filled with double-quantum vortex lines.

the velocity with which the information about an instability event travels to the NMR spectrometers, *i.e.* by the expansion of the newly formed B-phase vortices from the AB interface to the NMR region. A single vortex line expands in vortex-free rotation such that it extends from the AB interface as a rectilinear line along the cylinder axis to its curved end which connects to the cylinder wall. The curved end precesses in spiral motion, moving away from the AB interface towards increasing counterflow. The velocity of the spiral motion is largely determined by that section of the vortex end which is perpendicular to the cylinder wall [43]. Its velocity has the axial and azimuthal components

$$\boldsymbol{v}_L = -\alpha\,\Omega\,R\,\hat{\boldsymbol{z}} - (1-\alpha')\,\Omega\,R\,\hat{\boldsymbol{\phi}}\,, \qquad (14)$$

where $\alpha(T)$ and $\alpha'(T)$ are the dissipative and reactive mutual friction coefficients. Thus the axial expansion time is $\Delta t \approx d/(\alpha\Omega R)$ for bridging the distance d from the AB interface to the NMR coil. This estimate is a good approximation even in the case when many vortices are expanding simultaneously. At high temperatures, for instance at $0.85\,T_c$ at 29 bar pressure where the AB interface is in thermodynamic equilibrium, the delay Δt is a few seconds, but below $0.2\,T_c$ in the regime of ballistic quasiparticle motion where $\alpha(T)$ tends exponentially towards zero, Δt is more than an hour.

In a measurement where rotation is increased at a constant rate $d\Omega/dt = \dot\Omega$, the apparent measured critical velocity Ω_c^* is shifted higher by the equivalent of the delay,

$$[\Omega_c^*]^2 = \Omega_c^2 + \frac{2d}{\alpha\,R}\dot\Omega\,. \qquad (15)$$

In Fig. 5 an example is shown where $\Omega_c^{*^2}$ is plotted at different accelerations $\dot\Omega$, starting from a minimum rate of $10^{-4}\,\mathrm{rad/s^2}$. The intercept at $\dot\Omega = 0$ gives the true critical value $\Omega_c = 1.34\,\mathrm{rad/s}$, while from the slope $2d/(\alpha R)$ one obtains the mutual friction damping of vortex motion $\alpha = 1.1$ at 1.76 mK, which is in good agreement with other measurements. This 'flight-time' corrected method of identifying Ω_c works well for accelerations up to $\dot\Omega \sim 0.01\,\mathrm{rad/s^2}$.

The spiralling vortex motion in the long rotating cylinder becomes most interesting in the turbulent regime below $0.6\,T_c$ (see eg. [45]). Here the KH instability is followed by a sudden turbulent burst when the vortex loops transferred across the AB interface interact by reconnecting [11]. The burst takes place in the vicinity of the AB interface within a space comparable to the cylinder radius R. It boosts the number of the spiralling vortices close to that in equilibrium solid-body rotation, $N_{\mathrm{eq}} = \pi R^2\,2\Omega/\kappa$, removing thereby the excess rotating counterflow in this short section of the cylinder. Vortex expansion into the vortex-free flow then takes place within a spiralling turbulent vortex front with an axial length $\sim R$ [11]. Behind the front the vortices are close to a state of solid-body rotation. However, instead of an array of rectilinear lines, the vortices behind the front form a twisted bundle [46]. The open questions are concerned with the front dynamics in the zero temperature limit below $0.2\,T_c$ [44, 47].

In principle, Ω_c can be located by sweeping one of the variables Ω, T, P or I_b. In practice, three different techniques have been used. 1) The measurement in Fig. 5 is the most straightforward for locating Ω_c. Most of the data in this report were measured this way. Here Ω is increased from zero until the first vortices are detected in B phase, using constant slow acceleration. 2) Since $\Omega_c(T, P, I_b)$ is highly predictable and often already approximately known, a more accurate technique is a rapid increase across Ω_c by an increment which can be as small as $\Delta\Omega \sim 0.02\,\mathrm{rad/s}$ (consult Fig. 4), followed by rotation at constant Ω over a long waiting time exceeding the duration of the spiral motion. The waiting time can be used for monitoring the NMR line shape, to correct for drifts. 3) Since the heat leak to the sample depends on the rotation velocity [44], drifts can be reduced by scanning instead of Ω the barrier current I_b, *i.e.* by sweeping the current slowly downward until the AB interface becomes unstable in the reduced gradient $\sim dH_z/dz$. (Note that the superconducting magnets around the sample cylinder in Fig. 2 are thermally anchored to the mixing chamber and not to the nuclear cooling stage.)

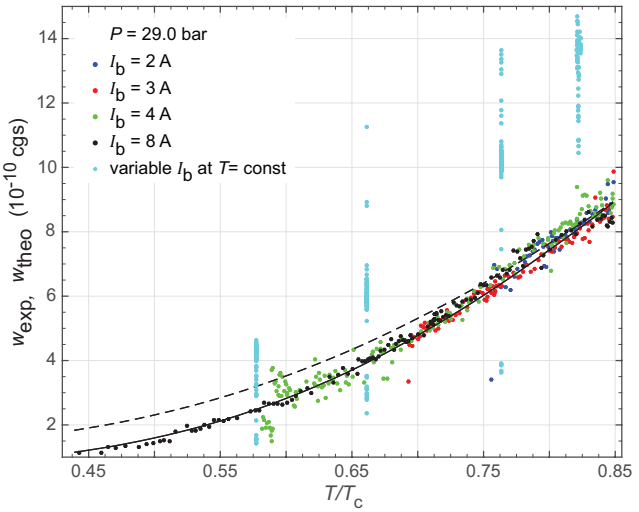

FIG. 6: KH measurements at 29.0 bar pressure. The experimental part $w_{\rm exp}$ from Eq. (5) is plotted as a function of temperature $T/T_{\rm c}$ for the measured data. The majority of the data comes from measurements of $\Omega_{\rm c}$ as function of temperature at fixed barrier-magnet current $I_{\rm b}$. The vertical sets of data points represent measurements at constant temperature as a function of $I_{\rm b}$. The dashed and solid-line curves correspond to $w_{\rm theo}$ calculated without and with the fitted magnetic field dependence of the surface tension, respectively.

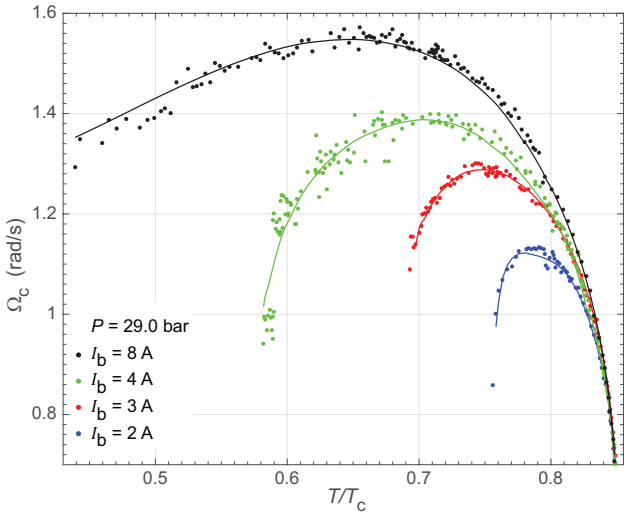

FIG. 7: KH rotation velocity $\Omega_{\rm c}(T)$ at 29 bar. The rotation velocity of the first KH instability event is recorded and plotted here, obtained while rotation is slowly increased from zero at constant T, P, and $I_{\rm b}$. Temperature is changed incrementally from one constant value to the next. The different sets of data respresent measurements at different fixed currents $I_{\rm b}$. The $I_{\rm b} = 2$ A, 3 A, and 4 A curves terminate at low temperatures where the AB interface is not maintained at these currents. The solid-line curves represent the result from fitting the magnetic field dependence.

V. KH MEASUREMENTS

Fig. 6 illustrates measurements of the KH critical rotation velocity $\Omega_{\rm c}(T, I_{\rm b})$, by plotting $w_{\rm exp}(T)$ (from Eq. (5)) as a function of temperature at a fixed pressure of 29 bar. In Fig. 7 the majority of the same data is plotted as $\Omega_{\rm c}$ versus temperature. These curves have the generic "umbrella" shape, which starts at high pressures ($P > 21.2$ bar) from $T_{\rm AB}$ or at low pressures from $T_{\rm c}$. Towards low temperatures at large $I_{\rm b}$ the curve flattens out towards a constant, while at smaller $I_{\rm b}$ the AB interface might not be maintained at low temperatures and the curve plummets down to a termination point.

The shape of the curves can be understood by considering the field distribution of the cylindrical barrier solenoid: 1) With decreasing temperature the critical field $H_{\rm AB}$ increases approximately parabolically and the AB interface settles down along the field contour $H(r, z) = H_{\rm AB}(T, P)$. At fixed large $I_{\rm b}$ the location $z_{\rm AB}$ of the AB interface moves with decreasing temperature closer to the magnet center and the field gradient increases. The measurements at $I_{\rm b} = 7$ A represent this behavior where the data ultimately at the lowest temperatures tend towards a constant value. 2) At lower $I_{\rm b}$ the AB interface ultimately reaches the inflection point in the field distribution at some temperature. Below this temperature the gradient $\mid \nabla H \mid_{z=z_{\rm AB}}$ starts decreasing, until at some low temperature limit the magnetic force F becomes too weak to maintain the interface. This behavior is exemplified by the data measured at 2 A, 3 A, and 4 A.

In the plot of $w_{\rm exp}(T)$ in Fig. 6 all this data collapses on one common curve which at high pressures is monotonously decreasing with decreasing temperature. At low pressures, where the zero-field $T_{\rm AB}$ moves to $T_{\rm c}$, the curve displays an initial steep rise just below $T_{\rm c}$, where the rapid increase in $\Omega_{\rm c}(T)$ first dominates, before settling down on a slowly descending dependence with decreasing temperature.

The vertical columns of data points in Fig. 6 represent measurements at constant temperature (and thus fixed $H_{\rm AB}$), while the current $I_{\rm b}$ is varied. They display the range of variation in $w_{\rm exp}$ obtainable with the present barrier solenoid where the maximum operating current in the CuNi-clad filamentary NbTi superconducting wire is limited to 8 A. This limits the maximum of the vertical column, which corresponds to the situation when $z_{\rm AB}$ is furthest away from the magnet center (well beyond the inflection point of the field distribution $H_z(z)$). At lower $I_{\rm b}$, $z_{\rm AB}$ resides closer to the magnet center. The bottom end of the column corresponds to the lowest current $I_{\rm b}$ at which the magnetic restoring force $\propto H_{\rm AB}(T) \mid \nabla H \mid_{z=z_{\rm AB}}$ still maintains an interface and $z_{\rm AB}$ is closest to the magnet center. Owing to the fixed upper limit $I_{\rm b} \leq 8$ A and the termination at low $I_{\rm b}$, which moves to higher $I_{\rm b}$ values when the temperature is lower, the height of the vertical data columns decreases towards low temperatures.

Hence both types of measurement series terminate in a

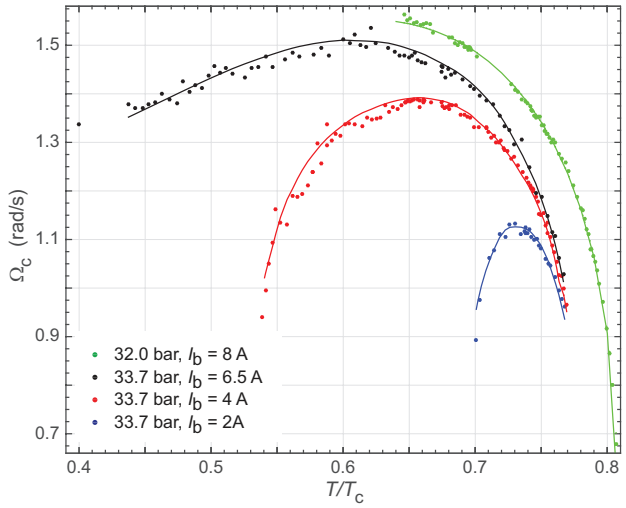

FIG. 8: Critical rotation velocity of KH instability at 32.0 and 33.7 bar. The same conventions are used as in Fig. 7. The 32.0 bar measurements were conducted after the solid ^{3}He plug in the fill line of the sample container had accidentally slipped. The slip reduced the pressure to an unknown value. The assignment (32.0 ± 0.25) bar was determined from the measured temperature of the B $\rightarrow$ A transition at zero field: $T_{\rm AB}/T_{\rm c} \simeq 0.81$.

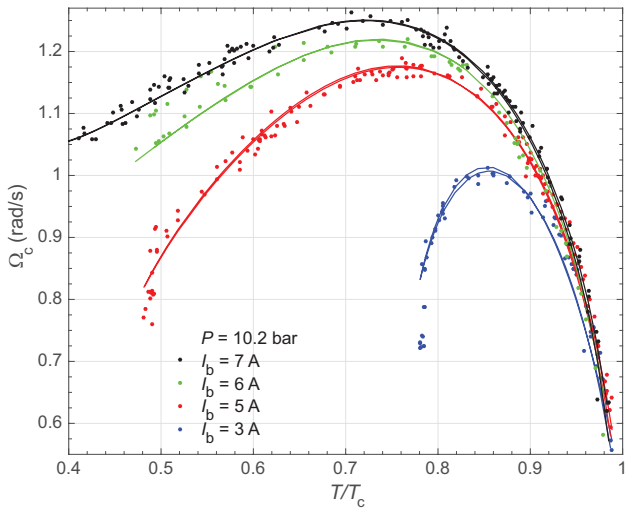

FIG. 9: KH rotation velocity at 10.2 bar. The higher pressure data in Figs. 8 and 7 were mainly collected in the AB configuration of phase stacking (Fig. 2), where the instability of only one AB interface can be recorded. The measurements at 10.2 bar and at zero pressure (Fig. 10) were performed in the BAB stacking configuration, where the independently occurring instabilities at the two AB interfaces were monitored.

collapse of the interface if the magnetic restoring force becomes too weak. Careful measurements around such termination points display more complex behavior than described above [42]. When the termination is approached from above, the thickness of the A-phase layer in Fig. 2 decreases until a hole is punched into the final thin A-phase membrane. In this final state, the A-phase volume collapses to a narrow annulus coating the cylinder wall, where the interface is still sustained by a slightly larger restoring force. Owing to this change in the topology of the AB interface and the associated barriers in nucleating the first order AB phase transition, $\Omega_{\rm c}(T, I_{\rm b})$ displays in the vicinity of a termination point both thermal and magnetic hysteresis. Thus around a termination point the $\Omega_{\rm c}$ data apear to show more scatter and lie below the regular dependence (see *eg.* the $I_{\rm b} = 4$ A data at low temperatures in Fig. 6).

Below we analyze the two types of measurements, examining first measurements at constant $I_{\rm b}$ and comparing the result then to measurements at constant T.

A. KH instability at constant magnet current

Results for $\Omega_{\rm c}(T)$ at fixed current $I_{\rm b}$ are shown in Figs. 7 - 10. In the figures the measured $\Omega_{\rm c}(T, P, I_{\rm b})$ is compared to its calculated estimate from

$$\Omega_{\rm c}(T) = \frac{1}{R_{\rm eff}} \left[4\, H_{\rm AB} \;\; |\nabla H|_{H_z = H_{\rm AB}} \; \frac{\sigma\, \Delta\chi}{\rho^2_{\rm s,eff}} \right]^{1/4} . \quad (16)$$

Taking currently accepted values for the different quantities at low magnetic fields one finds that this expression is in agreement with the data at high temperatures, but increasingly overestimates $\Omega_{\rm c}$ towards low temperatures, being above the measurements by about 10 % at $0.5\, T_{\rm c}$ at the pressures 10 – 34 bar. We attribute the deviation to the magnetic polarization of B phase at high $H_{\rm AB}(T)$ fields and associate the strongest field dependence with the surface tension.

The field dependence is analyzed using the following fitting procedure. The critical field $H_{\rm AB}(T, P)$ is taken from Ref. [48], the field gradient $\nabla H\,|_{H_z = H_{\rm AB}}$ is calculated from the information given for the barrier solenoid in Ref. [42], the B-phase susceptibility $\chi_{\rm B\perp}(T, P)$ is interpolated from the results measured by Scholz [49], and the superfluid densities $\rho_\parallel$ and $\rho_\perp$ are calculated numerically in the weak coupling approximation. The magnetic field dependences are thus approximately accounted for except in the surface tension.

The low-field surface tension is introduced in the form $\sigma(T, P) = \sigma_{\rm AB}(0, P)(1 - T/T_{\rm c})^{3/2}$, where we use a smooth polynomial for $\sigma_{\rm AB}(0, P)$ as a function of pressure. Its initial estimate is obtained by fitting the high temperature data at $H_{\rm AB} \leq 0.1$ T. The deviation of the low temperature data then proves to be parabolic: $\sigma(T, P, H_{\rm AB}) = \sigma_{\rm AB}(0, P)\; (1 - T/T_{\rm c})^{3/2}\; (1 - a H^2_{\rm AB})$. Since the experimental data sets at each pressure are quite sizeable, the final step was to improve the fitting by searching for an overall minimum squared deviation. The error analysis shows that the dominant uncertainty arises from locating the parameter values in the shallow minimum of the sum of the squared deviations. This in-

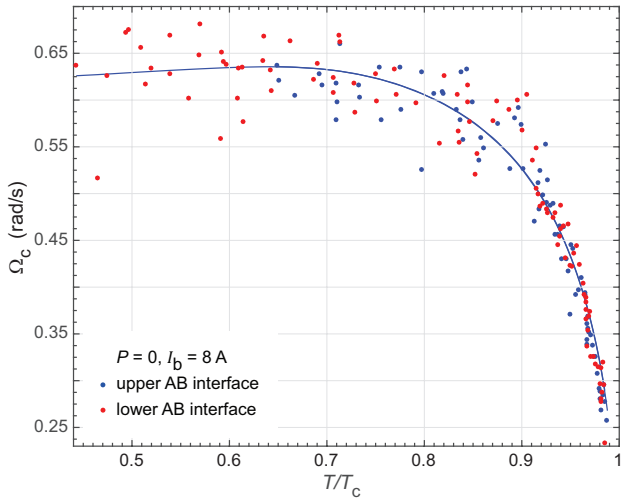

FIG. 10: KH rotation velocity at zero pressure. The instabilities of the two AB interfaces (see Fig. 2) occur independently and their critical velocities show no systematic deviations from a common dependence. The scatter is larger than at elevated pressures, owing to lower rotation velocities and smaller frequency shifts in the NMR measurement [34].

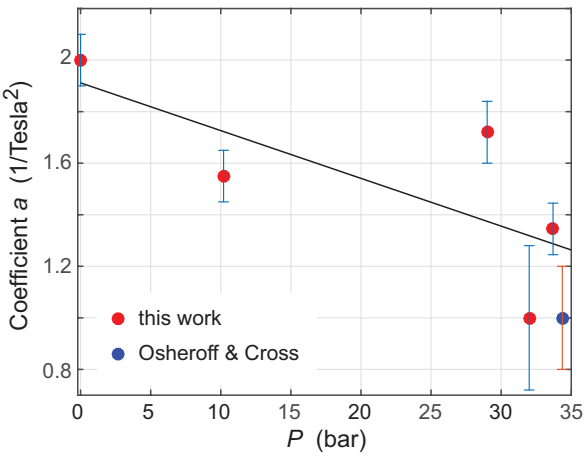

FIG. 11: Surface tension of AB interface in magnetic field. The coefficient a in the parabolic suppression of the surface tension with magnetic field is plotted at different sample pressures: $\sigma(T,P,H) = \sigma_{\rm AB}(0)\,(1-T/T_c)^{3/2}\,(1-aH^2)$. The fitted line corresponds to $a = 1.91 - 0.0185P/\mathrm{bar}$ (in Tesla^{-2}). The blue data point represents an average of the measurements in Ref. [51]. The error bars reflect the overall uncertainty in the fitting of the KH measurements.

troduces smaller uncertainty limits of a few percent for $\sigma_{\rm AB}(0,P)$ and larger for a, generally $\lesssim 10\,\%$.

While searching for the best value of $\sigma_{\rm AB}(0,P)$, it is actually the scale factor $\Omega_c \propto \sigma_{\rm AB}(0,P)^{1/4}\,/\,R_{\rm eff}$ which is being fitted. The only reported low temperature measurement of surface tension [50] gives $\sigma(0.15\,T_c, P=0) = (3.03 \pm 0.28) * 10^{-9}\,\mathrm{J/m^2}$ in a field of $H_{\rm AB} = 338\,\mathrm{mT}$. We use this value to adjust the fitted zero pressure scale factor and extract an effective radius of $R_{\rm eff} = 2.67\,\mathrm{mm}$. This number is in line with $R_{\rm eff} = 2.5\,\mathrm{mm}$ determined in Fig. 4 or with $R_{\rm eff} = 2.6\,\mathrm{mm}$ measured in Ref. [8]. Assuming $R_{\rm eff}$ to be essentially pressure independent we obtain a surface tension which is adequately represented with the polynomial $\sigma_{\rm AB}(0,P) \simeq (5.02 + 3.40P - 0.112P^2 + 0.00123P^3)\,10^{-9}\mathrm{J/m^2}$ (P in bar). The magnetic field dependence consistent with this polynomial is depicted in Fig. 11.

With this adjustment to the Lancaster value, our result for $\sigma_{\rm AB}(0,P)$ leaves a discrepancy with the surface tension measurement of Osheroff and Cross [51]: our extrapolated value at melting pressure in zero field and $T_{\rm AB} = 0.78\,T_c$ is 30 % smaller. The reason has not been identified. In contrast, it appears that a parabolic magnetic field correction with $a \simeq 1\mathrm{Tesla}^{-2}$ can be regarded to be consistent with the Osheroff - Cross data, as shown in Fig. 12. In Ref. [52] the consistency of the Osheroff - Cross results with Thuneberg's GL expansion of the surface tension is examined, by searching for a proper combination of strong-coupling corrected GL β parameters. Such curves have the temperature dependence of the black curve in Fig. 12. Temperatures as low as $\sim 0.5\,T_c$ are in general not adequately represented by a GL expansion and, in view of Fig. 12, we conclude that

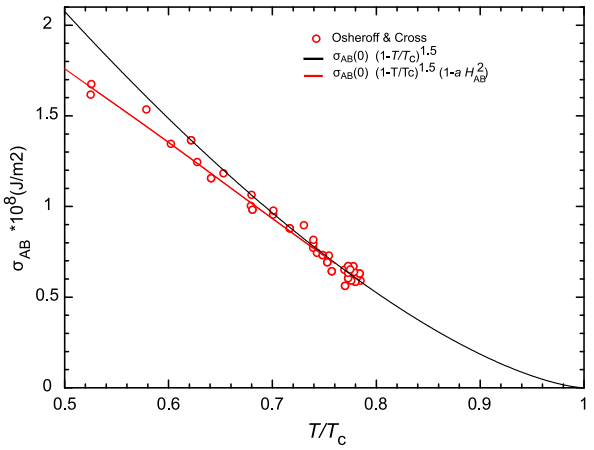

FIG. 12: Measurements of the AB interface surface tension at the melting pressure (34.4 bar) in Ref. [51]. The black curve represents $\sigma(T) = 5.87 * 10^{-8}\,(1-T/T_c)^{3/2}$, a fit for the data points with $T > 0.76\,T_c$. The red curve includes the magnetic field correction in Fig. 11.

the low temperature data points should be excluded from the fitting in Ref. [52], to account for the dependence on the magnetic field $H_{\rm AB}(T)$. This improves the fitting in Ref. [52].

In our measurements the A-phase section was generally prepared to contain the equilibrium number of doubly quantized vortices which have a continuous order parameter distribution with no singular central line defect [7]. For reference in some cases also the equilibrium vortex sheet was grown. This is a related structure, also with continuous order parameter distribution [40]. Within the

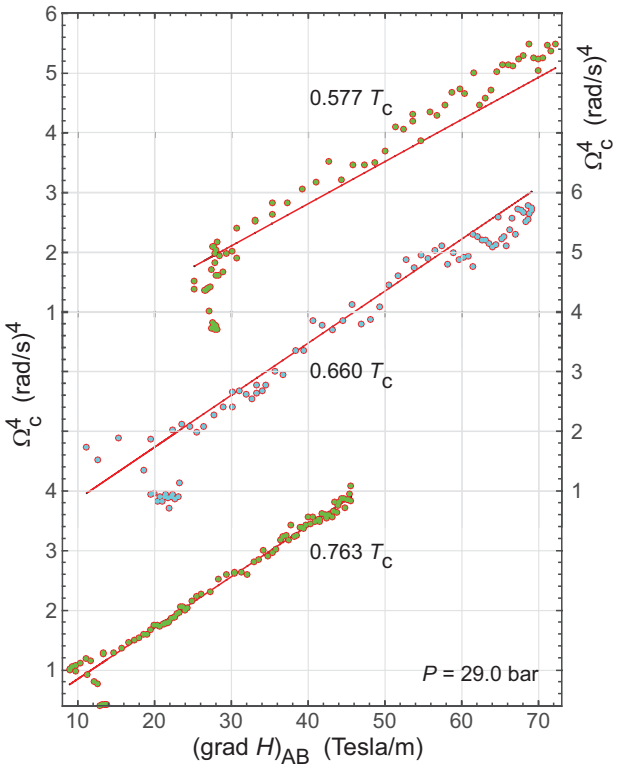

FIG. 13: KH instability measured at constant temperature as a function of the current I_b in the barrier magnet at 29.0 bar. At all three temperatures the low-current termination includes data points where the A phase volume is not a singly connected complete layer. The lines represent Eq. (16). (Note that the vertical scales of the two upper data sets have been moved upward).

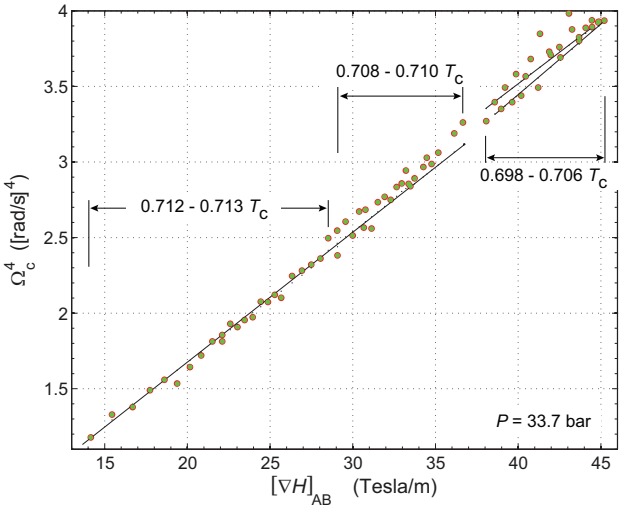

FIG. 14: KH instability measured at a constant temperature of $\sim 0.70\,T_c$ at 33.7 bar. The data was collected in three separate measuring sessions within slightly differing temperature ranges, as indicated in the plot. The lines display the low-field instability in Eq. (16), calculated at the temperature of each measured data point.

experimental scatter $\Omega_c(T)$ was found to be unaffected by the choice of the A-phase vortex structure. This conclusion is expected: the instability in Eq. (3) depends on the tangential flow velocities at the interface which are not affected by the vortex structure if the flow conditions remain otherwise unchanged.

B. KH instability at constant temperature

In measurements at constant temperature as a function of I_b, $\Omega_c^4 \propto |\nabla H|_{z=z_{AB}}$ (Eq. (16)). Here the field H_{AB} stays constant, while the location z_{AB} of the AB interface moves further away from the magnet center in an increasing field gradient. We use this linear dependence with a temperature dependent slope as a consistency check of the data and the model. Examples measured at three different temperatures are shown in Fig. 13.

Such tests require accurate temperature control during the measurement of the slope. The instability can be traversed by sweeping Ω upward at constant I_b or by sweeping I_b downward at constant Ω. In both cases rotation has to be stopped after each instability event, to remove the vortices from the B phase sections and to initialize the measuring setup for the next round of measurements. As the heat leak and the warmup rate depend on Ω [53], maintaining precise temperature stability requires careful automation. This was not seriously attempted in the present measurements. An illustration is shown in Fig. 14. Here a 2 % variation in the measuring temperature is visible as a change in the slope of the linear dependence Ω_c^4 versus $\nabla H|_{z=z_{AB}}$ which would amount to a 5 % uncertainty in the determination of the slope.

A further concern might be magnetic remanence in superconducting materials, trapped inhomogeneous fields which contribute to the value of the field gradient. The most sensitive place to search for remanent flux motion is the vicinity of a low-current termination (see Ref. [42]). Sweeping I_b up and down does not affect the measured Ω_c within the scatter of the measurements, which means that any trapped flux would have to be strongly pinned. Nevertheless, it is possible that persistent remanent fields are trapped in the initial cool down of the apparatus while charging the various superconducting magnets. These could explain some of the more systematic deviations in Figs. 13 and 14.

VI. DISCUSSION

The superfluid KH instability of the AB interface takes place between two different states within the order parameter manifold of the ^{3}He superfluids. The interface resides in a magnetic field $H_{AB}(T,P)$ and is localized by a steep field gradient $|\nabla H|_{H_z=H_{AB}}$. The instability crite-

rion (3) explains the measurements at high temperatures $T/T_c > 0.7$, corresponding to $H_{AB} < 0.1$ Tesla. At low temperatures fields as large as $H \lesssim 0.6$ Tesla may be encountered and an increasing deviation opens up between measurement and criterion (3) calculated using low-field values. The magnetic polarization of the ^{3}He-B properties hence leads to a sizeable reduction in the interface stability.

Little quantitative information exists on the magnetic deformation of the energy gap and its influence on the properties responsible for the interface stability. The first attempt to increase agreement by considering the boundary conditions at the interface and changes in the B-phase order parameter texture as a function of the applied field showed [33] that the stability criterion had to be amended by a renormalized superfluid density Eq. (8).

At second inspection the magnetic-field-induced reduction in the surface tension proves to be more important. Its first-order parabolic correction with magnetic field has here been extracted from measurements at different pressures extending down to $0.4\,T_c$. It is found to be in good agreement with the value of surface tension measured by Bartkowiak *et al.* at zero pressure and $0.15\,T_c$. In principle the surface tension is calculable at low temperatures; the present results we hope provide an incentive for such comparison.

The measurements presented here extend down to $0.4\,T_c$. Can we safely extrapolate this picture of the KH instability to the zero temperature limit? This is a question which should be answered with measurements below $0.2\,T_c$, where the density of the thermal bulk liquid excitations is exponentially depleted to such an extent that the interface appears to become decoupled from the external reference frame. The interface stability is continuously probed by perturbations with amplitudes in the non-linear regime, *i.e.* their attempt amplitude must be comparable to the wave length λ of the interfacial wave to be formed. This amplitude is large, in the hierarchy of length scales at large magnetic fields $R \gg R - R_{\rm eff} \sim \lambda \gg \xi_H \gg \xi$, which makes a reconstruction of the time dependence for the formation of the instability a hard problem. We have experimentally monitored the time required for the instability to build up at temperatures down to $0.2\,T_c$. This will be discussed in a forthcoming report.

Acknowledgements:–We are indebted to the many generations of graduate students who contributed to this study. We thank our late colleague Nikolai Kopnin [26] for encouragement, similarly Erkki Thuneberg [38] and Grigori Volovik [6] for their interest. Financial support was provided by the Aalto School of Science, its research infrastructure Low Temperature Laboratory, and the Academy of Finland (Centers of Excellence Programme project no. 284594).

[1] Contact address e-mail: matti.krusius@aalto.fi

[2] H. Lamb, *Hydrodynamics* (Dover Publ., New York, 1932), Chap. IX; S. Chandrasekhar, *Hydrodynamic and Hydromagnetic Stability* (Oxford University Press, New York, 1961), Chap. XI; L.D. Landau and E.M. Lifshitz, *Fluid Mechanics* (Pergamon Press, 1989), Chap. VII.

[3] Lord Kelvin (Sir William Thomson) *Mathematical and physical papers*, Vol. **4**, *Hydrodynamics and General Dynamics*, Cambridge University Press, 1910.

[4] H.L.F. von Helmholtz, Monatsberichte der königlichen Akademie der Wissenschaften zu Berlin, 215 (1868).

[5] R. Blaauwgeers, V.B. Eltsov, G. Eska, A.P. Finne, R.P. Haley, M. Krusius, J.J. Ruohio, L. Skrbek, G.E. Volovik, *Shear flow and Kelvin-Helmholtz instability in superfluids*, Phys. Rev. Lett. **89**, 155301 (2002).

[6] G.E. Volovik, *On Kelvin-Helmholtz instability in superfluids*, JETP Lett. **75**, 491 (2002).

[7] R. Blaauwgeers, V.B. Eltsov, M. Krusius, J.J. Ruohio, R. Schanen, G.E. Volovik, *Double-quantum vortex in superfluid ^{3}He-A*, Nature **404**, 471 (2000).

[8] R. Hänninen, R. Blaauwgeers, V.B. Eltsov, A.P. Finne, M. Krusius, E.V. Thuneberg, G.E. Volovik, *Structure of surface vortex sheet between two rotating ^{3}He superfluids*, Phys. Rev. Lett. **90**, 225301, (2003).

[9] M. Krusius, E.V. Thuneberg, Ü. Parts, *A-B phase transition in rotating superfluid ^{3}He*, Physica B **197**, 376 (1994); Ü. Parts, Y. Kondo, J.S. Korhonen, M. Krusius, E.V. Thuneberg, *Vortex layer on the interface between the A and B phases in superfluid ^{3}He*, Phys. Rev. Lett. **71**, 2951 (1993); see also Ref. [20] Chap. 17.

[10] A.P. Finne, T. Araki, R. Blaauwgeers, V.B. Eltsov, N.B. Kopnin, M. Krusius, L. Skrbek, M. Tsubota, G.E. Volovik, *An intrinsic velocity-independent criterion for superfluid turbulence*, Nature **424**, 1022 (2003).

[11] V.B. Eltsov, A.I. Golov, R. de Graaf, R. Hänninen, M. Krusius, V.S. Lvov, R.E. Solntsev, *Quantum turbulence in a propagating superfluid vortex front*, Phys. Rev. Lett. **99**, 265301 (2007).

[12] A.P. Finne, S. Boldarev, V.B. Eltsov, M. Krusius, *Measurement of turbulence in superfluid ^{3}He-B*, J. Low Temp. Phys. **136**, 249 (2004).

[13] S.E. Korshunov, *Analog of the KelvinHelmholtz Instability on the free surface of a superfluid liquid*, JETP Lett. **75**, 423 (2002).

[14] S.N. Burmistrov, L.B. Dubovskii, T. Satoh, *Kelvin-Helmholtz instability and dissipation in a phase-separated ^{3}He-^{4}He liquid mixture*, J. Low Temp. Phys. **138**, 513 (2005).

[15] D. Kobyakov, A. Bezett, E. Lundh, M. Marklund, V. Bychkov, *Turbulence in binary Bose-Einstein condensates generated by highly nonlinear Rayleigh-Taylor and Kelvin-Helmholtz instabilities*, Phys. Rev. A **89**, 013631 (2014).

[16] E. Lundh, J.-P. Martikainen, *Kelvin-Helmholtz instability in two-component Bose gases on a lattice*, Phys. Rev. A **85**, 023628 (2012).

[17] N. Suzuki, H. Takeuchi, K. Kasamatsu, M. Tsubota, H. Saito, *Crossover between Kelvin-Helmholtz and counter-superflow instabilities in two-component Bose-Einstein condensates*, Phys. Rev. A **82**, 063604 (2010).

[18] A. Ohta, R. Kashiwa, H. Sakaguchi, *Vortex lattices generated by the Kelvin-Helmholtz instability in the Gross-Pitaevskii equation*, Phys. Rev. A **82**, 055602 (2010).

[19] G.E. Volovik, *Black-hole horizon and metric singularity at the brane separating two sliding superfluids*, JETP Lett. **76**, 240 (2002).

[20] G.E. Volovik, *The Universe in a helium droplet*, (Oxford Science Publications, edit. 2009), Chap. 27.

[21] A. Mastrano, A. Melatos, *Kelvin-Helmholtz instability and circulation transfer at an isotropic-anisotropic superfluid interface in a neutron star*, Mon. Not. R. Astron. Soc. **361**, 927 (2005).

[22] W.C.G. Ho, C.M. Espinoza, D. Antonopoulou, N. Andersson, *Pinning down the superfluid and measuring masses using pulsar glitches*, Sci. Adv. **1**, e1500578 (2015).

[23] V.B. Eltsov, R. Hänninen, M. Krusius, *Vortices and other topological defects in non-equilibrium phase transitions of superfluid ^3He*, Physica C **470**, 803 (2010).

[24] A.P. Finne, V.B. Eltsov, R. Hänninen, N.B. Kopnin, J. Kopu, M. Krusius, M. Tsubota, G.E. Volovik, *Dynamics of vortices and interfaces in superfluid ^3He*, Rep. Prog. Phys. **69**, 3157 (2006).

[25] A.J. Leggett, S.K. Yip, in *Helium 3*, ed. W.P. Halperin, L.P. Pitaevskii (North-Holland, Amsterdam, 1990).

[26] N.B. Kopnin, *Movement of the interface between the A and B phases in superfluid helium-3: linear theory*, Sov. Phys. JETP **65**, 1187 (1987).

[27] V.M.H. Ruutu, J. Kopu, M. Krusius, Ü. Parts, B. Plaçais, E.V. Thueberg, W. Xu, *Critical velocity of vortex nucleation in rotating superfluid ^3He-A*, Phys. Rev. Lett. **79**, 5058 (1997).

[28] V.M.H. Ruutu, Ü. Parts, J.H. Koivuniemi, N.B. Kopnin, M. Krusius, *Intrinsic and extrinsic mechanisms of vortex formation in superfluid ^3He-B*, J. Low Temp. Phys. **107**, 93 (1997).

[29] W. Janke, H. Kleinert, *Superflow in ^3He-B in the presence of a magnetic field at all temperatures*, Phys. Lett. **78A**, 363 (1980).

[30] N. Schopohl, *Magnetic field dependence of the Leggett angle, the susceptibility, and the longitudinal NMR of ^3He-B*, J. Low Temp. Phys. **49**, 347 (1982).

[31] M. Ashida, K. Nagai, *A-B transition of superfluid ^3He under magnetic field at low pressures*, Prog. Theor. Phys. **74**, 949 (1985).

[32] S.N. Fisher, A.M. Guénault, C.J. Kennedy, G.R. Pickett, *Distortion of superfluid ^3He-B as a function of magnetic field and the first-order transition to ^3He-A at the $T = 0$ limit*, Phys. Rev. Lett. **67**, 1270 (1991). S.N. Fisher, *The mechanical properties of superfluids ^3He-A and ^3He-B in the ballistic regime*, Ph.D. thesis, Lancaster University (see in particular the table in the appendix of the thesis which lists the magnetic field dependence of $\Delta_\parallel$ and $\Delta_\perp$, as calculated by the authors of Ref. [31]).

[33] T. Ruokola, J. Kopu, *Kelvin-Helmholtz instability in anisotropic superfluids*, JETP Lett. **81**, 771 (2005).

[34] R. de Graaf, V.B. Eltsov, J.J. Hosio, P.J. Heikkinen, M. Krusius, *Textures of superfluid 3He-B in applied flow and comparison with hydrostatic theory*, J. Low Temp. Phys. **163**, 238 (2011).

[35] E.V.Thuneberg, *Hydrostatic theory of superfluid ^3He-B*, J. Low Temp. Phys. **122**, 657 (2001).

[36] P.J. Hakonen, M. Krusius, M.M. Salomaa, R.H. Salmelin, J.T. Simola, A.D. Gongadze, G.E. Vachnadze, G.A. Kharadze, *NMR and axial magnetic field textures in stationary and rotating superfluid 3He-B*, J. Low Temp. Phys. **76**, 225 (1989).

[37] M. Arrayás, S.N. Fisher, R.P. Haley, G.R. Pickett, M. Skyba, *Orbital damping of the oscillating superfluid ^3He A–B interface at low temperatures*, J. Low Temp. Phys. **175**, 706 (2014).

[38] E.V. Thuneberg, *A-B interface of superfluid ^3He in a magnetic field*, Phys. Rev. B **44**, 9685 (1991).

[39] R. Kaul, H. Kleinert, *Surface energy and textural boundary conditions between A and B phases of ^3He*, J. Low Temp. Phys. **38**, 539 (1980).

[40] Ü. Parts, E.V. Thuneberg, G.E. Volovik, J.H. Koivuniemi, V.M.H. Ruutu, M. Heinilä, J.M. Kairimäki, M. Krusius, *Vortex Sheet in rotating superfluid ^3He-A*, Phys. Rev. Lett. **72**, 3839 (1994).

[41] R. Blaauwgeers, V.B. Eltsov, A.P. Finne, M. Krusius, J.J. Ruohio, *Magnetically stabilized AB interface in rotating superfluid ^3He*, Physica B **329-333**, Part 1, 93 (2003).

[42] V.B. Eltsov, R. Blaauwgeers, A.P. Finne, M. Krusius, J.J. Ruohio, G.E. Volovik, *Instability of AB interfaces of different shapes in rotating 3He-B*, Physica B 329-333, Pt. 1, 96 (2003).

[43] A.P. Finne, V.B. Eltsov, R. Blaauwgeers, Z. Janu, M. Krusius, L. Skrbek, *Time of flight measurements on quantized vortex lines in rotating ^3He-B*, J. Low Temp. Phys. **134**, 375 (2004).

[44] J.J. Hosio, V.B. Eltsov, R. de Graaf, P.J. Heikkinen, R. Hänninen, M. Krusius, V.S. L'vov, G.E. Volovik, *Superfluid vortex front at $T \to 0$: Decoupling from the reference frame*, Phys. Rev. Lett. **107**, 135302 (2011).

[45] V.B. Eltsov, R. Hänninen, M. Krusius, *Quantum turbulence in superfluids with wall-clamped normal component*, Proc. Natl. Acad. Sci. **111**, Suppl. 1, 4711 (2014).

[46] V.B. Eltsov, A.P. Finne, R. Hänninen, J. Kopu, M. Krusius, M. Tsubota, and E.V. Thuneberg, *Twisted vortex state*, Phys. Rev. Lett. **96**, 215302 (2006).

[47] J.J. Hosio, V.B. Eltsov, P.J. Heikkinen, R. Hänninen, M. Krusius, V.S. Lvov, *Energy and angular momentum balance in wall-bounded superfluid turbulence at very low temperatures*, Nature Comm. **4**, 1614 (2013).

[48] I. Hahn, S.T.P. Boyd, H.M. Bozler, C.M. Gould, *Thermodynamic magnetization discontinuity at the A-B transition in superfluid ^3He*, Phys. Rev. Lett. **81**, 618 (1998); see also the 3He Calculator at the web site http://spindry.phys.northwestern.edu/he3.htm

[49] H.N. Scholz, PhD Thesis, Ohio State University (1981); R.F. Hoyt, H.N. Scholz, D.O. Edwards, *Superfluid ^3He-B: the dependence of the susceptibility and energy gap on magnetic field*, Physica B **107**, 287 (1981).

[50] M. Bartkowiak, S.N. Fisher, A.M. Guénault, R.P. Haley, G.R. Picket, P. Skyba, *Interfacial energy of the superfluid ^3He A-B phase interface in the zero-temperature limit*, Phys. Rev. Lett. **93**, 045301 (2004).

[51] D.D. Osheroff, M.C. Cross, *Interfacial surface energy between the superfluid phases of ^3He*, **38**, 905 (1977).

[52] H. Choi, J.P. Davis, J. Pollanen, T.M. Haard, W.P. Halperin, *Strong coupling corrections to the Ginzburg-Landau theory of superfluid ^3He*, Phys. Rev. B **75**, 174503 (2007). Consult Fig. 3 on p. 174503-7.

[53] J.J. Hosio, V.B. Eltsov, R. de Graaf, M. Krusius, J. Mäkinen, D. Schmoranzer, *Propagation of thermal ex-*

citations in a cluster of vortices in superfluid ^3He, Phys. Rev. B **84**, 224501 (2011).